Supplement of Atmos. Chem. Phys., 23, 2859–2875, 2023
https://doi.org/10.5194/acp-23-2859-2023-supplement

Supplement of

Comparison of aqueous secondary organic aerosol (aqSOA) product distributions from guaiacol oxidation by non-phenolic and phenolic methoxybenzaldehydes as photosensitizers in the absence and presence of ammonium nitrate

Brix Raphael Go et al.

Correspondence to: Chak K. Chan (chak.k.chan@cityu.edu.hk)

Section S1. UHPLC-PDA analyses

An ultra-high performance liquid chromatography system (UHPLC, Waters Acquity H-Class, Waters, Milford, USA) coupled to a photodiode array (PDA) detector (Waters, Milford, USA) was used for the quantification of GUA, DMB, and VL concentrations. The samples were first filtered through a 0.2 μm Chromafil® Xtra PTFE filter (Macherey-Nagel GmbH & Co. KG, Germany). The separation of products was conducted using an Acquity HSS T3 column (1.8 μm, 2.1 mm × 100 mm; Waters Corp.). The column oven was held at 30 °C, and the autosampler was cooled at 4 °C. The injection volume was set to 5 µL. The binary mobile phase was composed of water (A) and acetonitrile (B). The gradient elution was performed at a flow rate of 0.2 mL/min: 0–1 min, 10% eluent B; 1–25 min, linear increase to 90% eluent B; 25–29.9 min, hold 90% eluent B; 29.9–30 min, decrease to 10% eluent B; 30–35 min, re-equilibrate at 10% eluent B for 5 min. GUA, DMB, and VL were analyzed using the channels with UV absorption at 274, 274, and 300 nm, respectively.

Section S2. UHPLC-HESI-Orbitrap-MS analyses

A Thermo Orbitrap Fusion Lumos Mass Spectrometry (Thermo Fisher Scientific, Waltham, MA, USA) connected to a Thermo Scientific UltiMate 3000 UHPLC system (Thermo Fisher Scientific, Waltham, MA, USA) via heated electrospray ionization (HESI) as the interface (UHPLC-HESI-Orbitrap-MS) was used to characterize the reaction products. The mobile phases used were 0.1% (v/v) formic acid (in milli-Q water) (A) and acetonitrile (B). The same settings (e.g., column, gradient, oven temperature) used in the UHPLC-PDA (Sect. S1) were applied in the UHPLC-HESI-Orbitrap-MS system. The HESI-MS spectra were acquired in both positive and negative ion modes. The HESI parameters were as follows: Spray voltage, 2500 V for both positive and negative HESI; sheath gas, 35 arbitrary units; nebulizer auxiliary gas, 10 arbitrary units; sweep gas, 3 arbitrary units. General instrumental parameters were set as follows: ion transfer tube temperature, 320 °C; vaporizer temperature, 350 °C. The mass range for full scan MS was set at 50-1000 m/z with a mass resolution of 60,000 at 200 m/z. The automatic gain control (AGC) target was 4.0×10^5 with a maximum injection time of 50 ms. The UHPLC-HESI-Orbitrap-MS data obtained in positive and negative ion modes were pretreated using Progenesis QI (version 2.4; Nonlinear Dynamics) for peak picking and alignment. Most peaks detected in the blank (~99% for all experiments) were excluded from the samples except for peaks with a minimum of 2.5 times greater intensity in the sample spectrum than in the blank (Laskin et al., 2014). In addition, a peak was considered a product if the difference in the peak area between the samples before and after irradiation is ≥10 times. In this work, two independently prepared samples for each reaction condition were analyzed using the UHPLC-HESI-Orbitrap-MS. Only peaks that were reproducibly detected in both sets of samples were retained. The formula assignments were carried out using the MIDAS molecular formula calculator (http://magnet.fsu.edu/~midas/) with the following constraints: C ≤100, H ≤150, O ≤30, and N ≤10, and mass error of 10 ppm. The nitrogen atom was excluded in the constraints for experiments without AN. The ChemSpider database (Royal Society of Chemistry) was also queried to return valid molecules that may be useful for proposing product structures. Overall, the proposed structures in this work are based on the molecular formulas, DBE values, and structural and mechanistic information provided in earlier similar works on methoxyphenols (Yee et al., 2013; Li et al., 2014; Yu et al., 2014, 2016; He et al., 2019; Chen et al., 2020; Jiang et al., 2021; Misovich et al., 2021; Mabato et al., 2022). For clarity, the formulas discussed in this work correspond to neutral analytes (e.g., with H^+ or NH_4^+ removed from the ion formula).

The double bond equivalent (DBE) values (Koch and Dittmar, 2006) and carbon oxidation state (OS_C; Kroll et al., 2011, 2015; Lv et al., 2016) of the neutral formulas were calculated using the following equations:

$$\mathrm{DBE} = \mathrm{C} - \mathrm{H}/2 + \mathrm{N}/2 + 1 \qquad \text{(Eq. S1)}$$

$$\mathrm{OS_C} = 2 \times \mathrm{O}/\mathrm{C} + 3 \times \mathrm{N}/\mathrm{C} - \mathrm{H}/\mathrm{C} \qquad \text{(Eq. S2)}$$

where C, H, O, and N correspond to the number of carbon, hydrogen, oxygen, and nitrogen atoms in the neutral formula. Moreover, the average oxygen to carbon (O:C) ratios, ⟨O:C⟩: ($\langle \mathrm{O{:}\,C} \rangle = \sum_i(\mathrm{abundance_i})O_i / \sum_i(\mathrm{abundance}_i)C_i$), average nitrogen to carbon (N:C) ratios, ⟨N:C⟩: ($\langle \mathrm{N{:}\,C} \rangle = \sum_i(\mathrm{abundance_i})N_i / \sum_i(\mathrm{abundance}_i)C_i$), and average hydrogen to carbon (H:C) ratios, ⟨H:C⟩: ($\langle \mathrm{H{:}\,C} \rangle = \sum_i(\mathrm{abundance}_i)H_i / \sum_i(\mathrm{abundance_i})C_i$) after the reactions were further estimated using the signal-weighted method (Bateman et al., 2012). The average $\mathrm{OS_C}$, $\langle \mathrm{OS_C} \rangle$ was also calculated as follows:

$$\langle \mathrm{OS_C} \rangle = 2 \times \langle \mathrm{O{:}C} \rangle + 3 \times \langle \mathrm{N{:}C} \rangle - \langle \mathrm{H{:}C} \rangle \qquad \text{(Eq. S3)}$$

Section S3. IC analyses of small organic acids

An ion chromatography system (IC, Dionex ICS-1100, Sunnyvale, CA) equipped with a Dionex AS-DV autosampler (Sunnyvale, CA) enabled the analyses of small organic acids. The separation was achieved using an IonPac$^{\mathrm{TM}}$ AS11 column (4 × 250 mm) with an IonPac$^{\mathrm{TM}}$ AG11 guard column (4 × 50 mm). The isocratic elution was applied at a 1.0 mL/min flow rate with 12 mM sodium hydroxide (NaOH) as the eluent. The total run time was set at 10 min. The standard solutions (1–50 μM) of formic, succinic, and oxalic acid were analyzed three times along with the samples and water blank. Formic, succinic, and oxalic acid had retention times of 1.9 min, 3.7 min, and 5.9 min, respectively.

Section S4. UV-Vis spectrophotometric analyses

A UV-Vis spectrophotometer (UV-3600, Shimadzu Corp., Japan) was used to measure the absorbance changes for the samples. The absorbance values from 200 to 700 nm were measured instantly after sample collection, and measurements were done in triplicate. The change in the integrated area of absorbance from 350 to 550 nm was used to represent the absorbance enhancements. The increase of light absorption at this wavelength range, where GUA did not initially absorb light and where DMB and VL have little absorption, suggests the formation of light-absorbing products (Smith et al., 2016).

Section S5. Further discussions on van Krevelen diagrams and OS_c vs. n_C plots for GUA+DMB and GUA+VL aqSOA

Consistent with the higher contribution of ring-opening species, GUA+DMB had more products with H:C ≥1.5 and O:C ≤0.5 (Fig. S5a–b), possibly due to more oxygenated aliphatic species. GUA+VL (Fig. S5c–d) also had high-relative-abundance products with H:C of ~1 and O:C ≥0.5. Similar to our previous work (0.1 mM GUA + 0.1 mM VL; Mabato et al., 2022), the two high-relative-abundance species with O:C ≥0.5 were associated with hydroxylated products ($C_7H_8O_4$ and $C_8H_8O_5$, #28 and 35; Table S2) that were also observed in earlier works on $^3DMB^*$ and $^{\bullet}OH$-mediated oxidation (Yu et al., 2014, 2016). These hydroxylated products were also present in GUA+DMB but with lower relative abundance. Triplet-mediated phenol oxidation can generate H_2O_2 (Anastasio et al., 1997), a photolytic source of $^{\bullet}OH$. Indeed, hydroxylation is significant in aqueous-phase phenol oxidation (Li et al., 2014; Yu et al., 2014, 2016; Chen et al., 2020; Jiang et al., 2021; Misovich et al., 2021; Mabato et al., 2022).

The OS_C vs. n_C plots for both GUA+DMB and GUA+VL display high-relative-abundance species clustered at n_C of 12 to 15 and OS_C >-1, which can be ascribed to dimers and derivatives (Fig. S6a–d). The species with n_C >15 had the highest DBE values and can be attributed to trimers. These compounds were more abundant in GUA+DMB, likely due to the greater extent of photosensitized reactions by $^3DMB^*$ compared to $^3VL^*$. Indeed, oligomerization is an important process in aqSOA formation via triplet-mediated oxidation (Yu et al., 2014, 2016; Chen et al., 2020; Jiang et al., 2021; Misovich et al., 2021; Mabato et al., 2022). As indicated by the higher quantity of low DBE species, ring-opening and fragmentation pathways were more extensive in GUA+DMB. In GUA+VL, there were also high-relative-abundance products with n_C <10, $OS_C \geq 0$, and DBE <5, corresponding to the hydroxylated products mentioned earlier.

Section S6. Estimation of the apparent quantum efficiency of guaiacol photodegradation

The apparent quantum efficiency of GUA photodegradation (φ_{GUA}) in the presence of DMB, VL, or nitrate during simulated sunlight illumination can be defined as (Anastasio et al., 1997; Smith et al., 2014, 2016):

$$\Phi_{\mathrm{GUA}} = \frac{\text{mol GUA destroyed}}{\text{mol photons absorbed}} \qquad \text{(Eq. S4)}$$

Φ_{GUA} was calculated using the measured rate of GUA decay and rate of light absorption by DMB, VL, or nitrate through the following equation:

$$\Phi_{\mathrm{GUA}} = \frac{\text{rate of GUA decay}}{\text{rate of light absorption by DMB or VL or nitrate}} = \frac{k'_{\mathrm{GUA}} \times [\mathrm{GUA}]}{\sum[(1-10^{-\varepsilon_{\lambda}[\mathrm{C}]l}) \times I'_{\lambda}]} \qquad \text{(Eq. S5)}$$

where k'_{GUA} is the pseudo-first-order rate constant for GUA decay, [GUA] is the concentration of GUA (M), ε_λ is the base-10 molar absorptivity (M^{-1} cm^{-1}) of DMB, VL, or nitrate at wavelength λ, [C] is the concentration of DMB, VL, or nitrate (M), l is the pathlength of the illumination cell (cm), and I'_λ is the volume-averaged photon flux (mol-photons L^{-1} s^{-1} nm^{-1}) determined from 2NB actinometry:

$$j(2\mathrm{NB}) = 2.303 \times \Phi_{2\mathrm{NB}} \times l \times \Sigma_{300\,nm}^{350\,nm}(\varepsilon_{2\mathrm{NB},\lambda} \times I'_{\lambda} \times \Delta\lambda) \qquad \text{(Eq. S6)}$$

where j(2NB) is the decay rate constant of 2-nitrobenzaldehyde (2NB), the chemical actinometer used to determine the photon flux in the aqueous photoreactor, $\Phi_{2\mathrm{NB},\lambda}$ and $\varepsilon_{2\mathrm{NB},\lambda}$ are the quantum yield (molecule $photon^{-1}$) and base-10 molar absorptivity (M^{-1} cm^{-1}) for 2NB, respectively, and Δλ is the wavelength interval between actinic flux data points (nm).

Section S7. Further discussions on van Krevelen diagrams and OS_c vs. n_C plots for GUA+DMB+AN, GUA+VL+AN, and GUA+AN aqSOA

The position of the CHO, CHON, and CHN species in the van Krevelen diagrams for GUA+DMB+AN and GUA+VL+AN broadly resembled those of CHO species in the absence of AN (Fig. S5). The CHON species for GUA+DMB+AN and GUA+VL+AN mostly had O:C ratios <0.7, consistent with previous studies on BBOA e.g., wheat straw burning in K-Puszta in the Great Hungarian Plain of Hungary, biomass burning at Canadian rural sites such as Saint Anicet, and BBOA from Amazonia (Schmitt-Kopplin et al., 2010; Claeys et al., 2012; Kourtchev et al., 2017).

The CHN species in GUA+DMB+AN and GUA+VL+AN appeared to have analogous H:C ratios. GUA+DMB+AN had ~2 times more CHON and CHN species than GUA+VL+AN, and there were more of these species with higher abundance in the former, indicating a greater extent of reactions with AN. The high-relative-abundance products for GUA+DMB+AN and GUA+VL+AN were similar to those in the absence of AN, except the hydroxylated products (e.g., $C_7H_8O_4$; #28; Table S2) previously mentioned for GUA+VL. Among the high-relative-abundance products for GUA+DMB+AN was a CHN species with H:C of ~0.8. For GUA+VL+AN, the high-relative-abundance products include two CHON species with O:C and H:C ratios of 0.3-0.6 and 0.6-0.8. The major difference between GUA+AN and GUA+DMB+AN/GUA+VL+AN was the presence of more high-relative-abundance CHON and CHN species (Fig. S9) in GUA+AN which can be expected given that AN was the only source of oxidants in this case. Compared to GUA+AN, more species (CHO, CHON, and CHN) were observed for GUA+DMB+AN and GUA+VL+AN, attributable to contributions from both photosensitization and (ammonium) nitrate photolysis.

Moreover, GUA+DMB+AN and GUA+VL+AN aqSOA had mainly similar features in the OS_C vs. n_C plots as those observed in the absence of AN (Fig. S6). GUA+DMB+AN and GUA+VL+AN aqSOA also had more CHON and CHN species with higher OS_C, n_C, and DBE (Fig. S6e–h) relative to GUA+AN (Fig. S10), indicating more conjugated N-containing compounds. For GUA+DMB+AN and GUA+VL+AN, the CHON and CHN species had a wider range of OS_C compared to CHO species (Fig. S6e–h). The high-relative-abundance species (n_C of 12 to 15 and OS_C >-1) corresponded to dimers and trimers similar to those noted in the absence of AN, along with some N-containing species. These include a CHN species with n_C of 13, OS_C ~0, and 11 DBE for GUA+DMB+AN, and 2 CHON species with n_C of 5 and 11, OS_C of 2.5 and 1, and 6 and 9 DBE for GUA+VL+AN.

Table S1. Possible structures of the major products detected from GUA+DMB using UHPLC-HESI-Orbitrap-MS operated in positive (POS) and negative (NEG) ion modes.

No.	GUA+DMB POS Molecular formula and exact mass	DBE	Possible structure	No.	GUA+DMB NEG Molecular formula and exact mass	DBE	Possible structure
1	$C_{14}H_{14}O_4$ (246.0892)	8	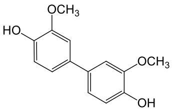	$C_{14}H_{14}O_4$ (246.0892) (No. 1; GUA+DMB POS)			
2	$C_{13}H_{10}O_3$ (214.0630)	9	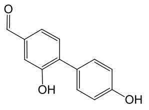	16	$C_{14}H_{14}O_6$ (278.0790)	8	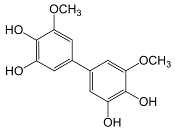
3	$C_{14}H_{12}O_4$ (244.0736)	9	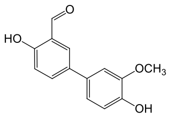	17	$C_{12}H_{10}O_4$ (218.0579)	8	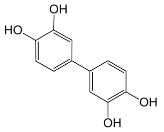
4	$C_{13}H_{10}O_4$ (230.0579)	9	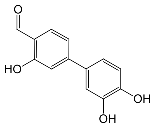	$C_{13}H_{12}O_4$ (232.0736) (No. 6; GUA+DMB POS)			
5	$C_{13}H_{10}O_5$ (246.0528)	9	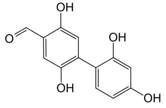	18	$C_7H_{10}O_5$ (174.0528)	3	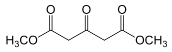
6	$C_{13}H_{12}O_4$ (232.0736)	8	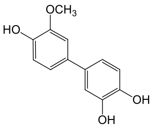	19	$C_{21}H_{18}O_8$ (398.1002)	13	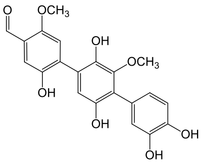
7	$C_{14}H_{12}O_5$ (260.0685)	9	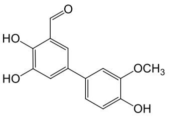	20	$C_{13}H_{12}O_6$ (264.0634)	8	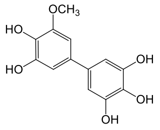
8	$C_{11}H_{12}O_5$ (224.0685)	6	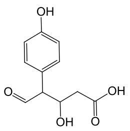	21	$C_{20}H_{18}O_6$ (354.1103)	12	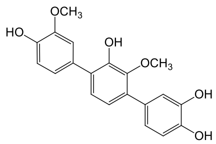
9	$C_{14}H_{12}O_7$ (292.0583)	9	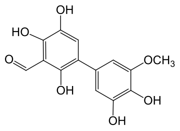	22	$C_{14}H_{14}O_7$ (294.0740)	8	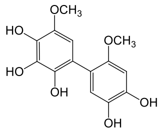
10	$C_{11}H_{14}O_6$ (242.0790)	5	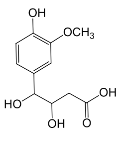	23	$C_{12}H_{14}O_4$ (222.0892)	6	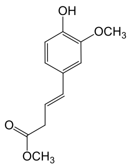

11	$C_{18}H_{18}O_7$ (346.1053)	10	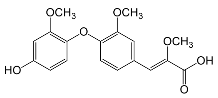	24	$C_{13}H_{10}O_6$ (262.0477)	9	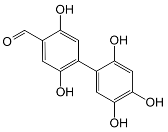
12	$C_{10}H_{12}O_3$ (180.0786)	5	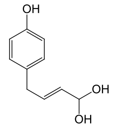	25	$C_{13}H_{14}O_4$ (234.0892)	7	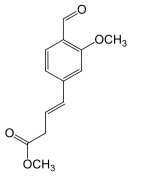
13	$C_7H_6O_4$ (154.0266)	5	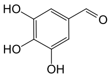	26	$C_{14}H_{14}O_5$ (262.0841)	8	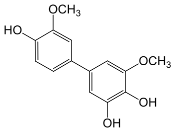
14	$C_{16}H_{18}O_6$ (306.1103)	8	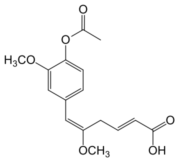	$C_{13}H_{10}O_5$ (246.0528) (No. 5; GUA+DMB POS)			
15	$C_7H_6O_5$ (170.0215)	5	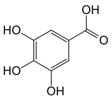	27	$C_{19}H_{16}O_6$ (340.0947)	12	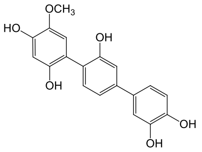

Table S2. Possible structures of the major products detected from GUA+VL using UHPLC-HESI- Orbitrap-MS operated in positive (POS) and negative (NEG) ion modes.

No.	GUA+VL POS Molecular formula and exact mass	DBE	Possible structure	No.	GUA+VL NEG Molecular formula and exact mass	DBE	Possible structure
28	$C_7H_8O_4$ (156.0423)	4	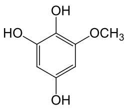	35	$C_8H_8O_5$ (184.0372)	5	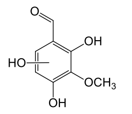
$C_{13}H_{10}O_4$ (230.0579) (No. 4; GUA+DMB, Table S1)				$C_{13}H_{12}O_4$ (232.0736) (No. 6; GUA+DMB, Table S1)			
$C_{13}H_{12}O_4$ (232.0736) (No. 6; GUA+DMB, Table S1)				$C_{14}H_{14}O_4$ (246.0892) (No. 1; GUA+DMB, Table S1)			
$C_{13}H_{10}O_5$ (246.0528) (No. 5; GUA+DMB, Table S1)				$C_{14}H_{14}O_6$ (278.0790) (No. 16; GUA+DMB, Table S1)			
29	$C_7H_8O_5$ (172.0372)	4	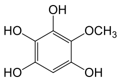	$C_{20}H_{18}O_6$ (354.1103) (No. 21; GUA+DMB, Table S1)			
30	$C_6H_6O_2$ (110.0368)	4	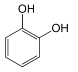	$C_{12}H_{10}O_4$ (218.0579) (No. 17; GUA+DMB, Table S1)			
31	$C_{10}H_{10}O_4$ (194.0579)	6	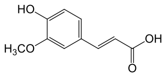	$C_6H_6O_2$ (110.0368) (No. 30; GUA+VL POS)			
32	$C_{11}H_8O_4$ (204.0423)	8	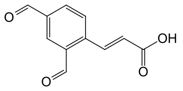	$C_7H_{10}O_5$ (174.0528) (No. 18; GUA+DMB, Table S1)			
33	$C_{12}H_{10}O_3$ (202.0630)	8	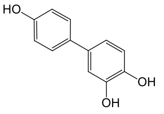	36	$C_{15}H_{14}O_5$ (274.0841)	9	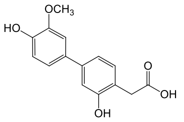
$C_{14}H_{12}O_5$ (260.0685) (No. 7; GUA+DMB, Table S1)				$C_{13}H_{12}O_6$ (264.0634) (No. 20; GUA+DMB, Table S1)			
$C_{13}H_{14}O_4$ (234.0892) (No. 25; GUA+DMB, Table S1)				37	$C_8H_8O_4$ (168.0423)	5	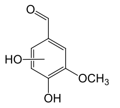
34	$C_{11}H_{10}O_6$ (238.0477)	7	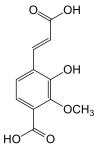	$C_{19}H_{16}O_6$ (340.0947) (No. 27; GUA+DMB, Table S1)			
$C_{13}H_{10}O_6$ (262.0477) (No. 24; GUA+DMB, Table S1)				$C_{11}H_{10}O_6$ (238.0477) (No. 34; GUA+VL POS)			
$C_{13}H_{12}O_6$ (264.0634) (No. 20; GUA+DMB, Table S1)				38	$C_5H_6O_5$ (146.0215)	3	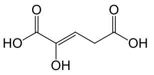
$C_7H_6O_4$ (154.0266) (No. 13; GUA+DMB, Table S1)				39	$C_6H_4O_4$ (140.0110)	5	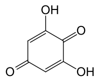

Table S3. Possible structures of the major products detected from GUA+DMB+AN using UHPLC-HESI-Orbitrap-MS operated in positive (POS) and negative (NEG) ion modes.

No.	GUA+DMB+AN POS Molecular formula and exact mass	DBE	Possible structure	No.	GUA+DMB +AN NEG Molecular formula and exact mass	DBE	Possible structure
$C_{14}H_{14}O_4$ (246.0892) (No. 1; GUA+DMB, Table S1)				$C_{13}H_{12}O_4$ (232.0736) (No. 6; GUA+DMB, Table S1)			
40	$C_{13}H_{10}N_4$ (222.0905)	11	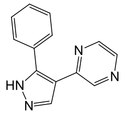	$C_{14}H_{14}O_6$ (278.0790) (No. 16; GUA+DMB, Table S1)			
$C_{13}H_{10}O_5$ (246.0528) (No. 5; GUA+DMB, Table S1)				$C_{14}H_{14}O_4$ (246.0892) (No. 1; GUA+DMB, Table S1)			
$C_{13}H_{10}O_4$ (230.0579) (No. 4; GUA+DMB, Table S1)				$C_{12}H_{10}O_4$ (218.0579) (No. 17; GUA+DMB, Table S1)			
41	$C_6H_6N_4$ (134.0592)	6	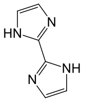	$C_{21}H_{18}O_8$ (398.1002) (No. 19; GUA+DMB, Table S1)			
$C_{13}H_{12}O_4$ (232.0736) (No. 6; GUA+DMB, Table S1)				$C_7H_{10}O_5$ (174.0528) (No. 18; GUA+DMB, Table S1)			
42	$C_{12}H_{11}N_3O_3$ (245.0800)	9	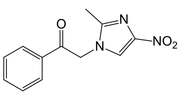	$C_{13}H_{12}O_6$ (264.0634) (No. 20; GUA+DMB, Table S1)			
43	$C_{10}H_8N_4O$ (200.0698)	9	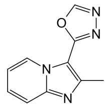	48	$C_{16}H_{14}N_6O_4$ (354.1076)	13	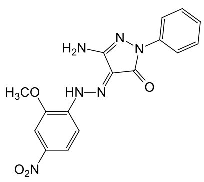
44	$C_6H_6N_4O$ (150.0542)	6	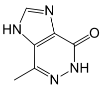	49	$C_{15}H_{10}N_4O_3$ (294.0753)	13	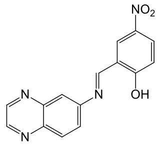
45	$C_{10}H_{14}N_4O_4$ (245.1015)	6	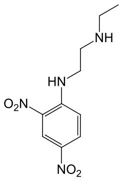	$C_{13}H_{10}O_6$ (262.0477) (No. 24; GUA+DMB, Table S1)			
46	$C_{13}H_{10}N_4O$ (238.0855)	11	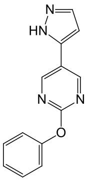	$C_{10}H_{10}O_4$ (194.0579) (No. 31; GUA+VL, Table S2)			
$C_{13}H_{12}O_6$ (264.0634) (No. 20; GUA+DMB, Table S1)				$C_7H_8O_4$ (156.0423) (No. 28; GUA+VL, Table S2)			
$C_7H_6O_4$ (154.0266) (No. 13; GUA+DMB, Table S1)				$C_{13}H_{14}O_4$ (234.0892) (No. 25; GUA+DMB, Table S1)			
$C_{12}H_{10}O_3$ (202.0630) (No. 33; GUA+VL, Table S2)				$C_{13}H_{10}O_5$ (246.0528) (No. 5; GUA+DMB, Table S1)			
47	$C_{13}H_8O_4$ (228.0423)	10	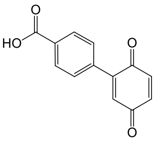	$C_{14}H_{14}O_5$ (262.0841) (No. 26; GUA+DMB, Table S1)			

Table S4. Possible structures of the major products detected from GUA+VL+AN using UHPLC-HESI-Orbitrap-MS operated in positive (POS) and negative (NEG) ion modes.

No.	GUA+VL+AN POS Molecular formula and exact mass	DBE	Possible structure	No.	GUA+VL+AN NEG Molecular formula and exact mass	DBE	Possible structure
$C_{14}H_{14}O_4$ (246.0892) (No. 1; GUA+DMB, Table S1)				$C_{13}H_{12}O_4$ (232.0736) (No. 6; GUA+DMB, Table S1)			
50	$C_{10}H_8O_2$ (160.0524)	7	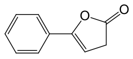	$C_{14}H_{14}O_6$ (278.0790) (No.16; GUA+DMB, Table S1)			
51	$C_{16}H_{18}O_4$ (274.1205)	8	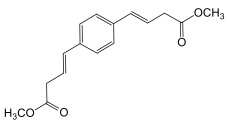	$C_{12}H_{10}O_4$ (218.0579) (No.17; GUA+DMB, Table S1)			
$C_{11}H_{12}O_5$ (224.0685) (No. 8; GUA+DMB, Table S1)				57	$C_{11}H_9N_3O_3$ (231.0644)	9	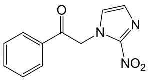
$C_{14}H_{12}O_5$ (260.068) (No. 7; GUA+DMB, Table S1)				$C_7H_{10}O_5$ (174.0528) (No.18; GUA+DMB, Table S1)			
$C_{12}H_{14}O_4$ (222.0892) (No. 23; GUA+DMB, Table S1)				$C_{15}H_{14}O_5$ (274.0841) (No. 36; GUA+VL, Table S2)			
52	$C_{11}H_{12}O_4$ (208.0736)	6	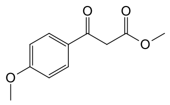	$C_{13}H_{12}O_6$ (264.0634) (No. 20; GUA+DMB, Table S1)			
$C_6H_6N_4O$ (150.0542) (No. 44; GUA+DMB+AN, Table S3)				58	$C_5H_6O_2$ (98.0368)	3	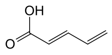
$C_{13}H_{12}O_4$ (232.0736) (No. 6; GUA+DMB, Table S1)				$C_{19}H_{16}O_6$ (340.0947) (No. 27; GUA+DMB, Table S1)			
53	$C_{12}H_8N_2O_3$ (228.0535)	10	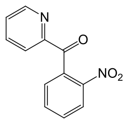	59	$C_{20}H_{16}O_7$ (368.0896)	13	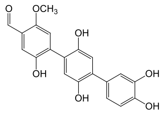
54	$C_{11}H_{14}O_4$ (210.0892)	5	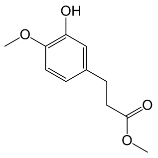	$C_{21}H_{18}O_8$ (398.1002) (No. 19; GUA+DMB, Table S1)			
$C_7H_6O_4$ (154.0266) (No. 13; GUA+DMB, Table S1)				$C_7H_6O_4$ (154.0266) (No. 13; GUA+DMB, Table S1)			
55	$C_{14}H_{12}O_6$ (276.0634)	9	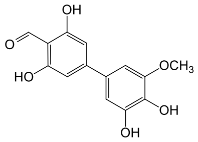	$C_{15}H_{10}N_4O_3$ (294.0753) (No. 49; GUA+DMB+AN, Table S3)			
56	$C_{14}H_{10}N_4O_7$ (346.0550)	12	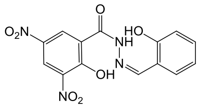	$C_{13}H_{10}O_6$ (262.0477) (No. 24; GUA+DMB, Table S1)			
$C_{13}H_{12}O_6$ (264.0634) (No. 20; GUA+DMB, Table S1)				$C_5H_6O_5$ (146.0215) (No. 38; GUA+VL, Table S2)			

Table S5. Possible structures of the major products detected from GUA+AN using UHPLC-HESI-Orbitrap-MS operated in positive (POS) and negative (NEG) ion modes.

<table>
<tr><th>No.</th><th>GUA+AN POS Molecular formula and exact mass</th><th>DBE</th><th>Possible structure</th><th>No.</th><th>GUA+AN NEG Molecular formula and exact mass</th><th>DBE</th><th>Possible structure</th></tr>
<tr><td colspan="4">$C_{13}H_{10}O_4$ (230.0579)
(No. 4; GUA+DMB, Table S1)</td><td colspan="4">$C_{14}H_{14}O_6$ (278.0790)
(No. 16; GUA+DMB, Table S1)</td></tr>
<tr><td colspan="4">$C_6H_6N_4O$ (150.0542)
(No. 44; GUA+DMB+AN, Table S3)</td><td>68</td><td>$C_{12}H_{19}N_3O$
(221.1528)</td><td>5</td><td>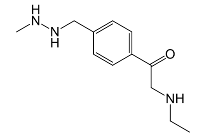</td></tr>
<tr><td colspan="4">$C_{11}H_{12}O_5$ (224.0685)
(No. 8; GUA+DMB, Table S1)</td><td colspan="4">$C_{12}H_{10}O_4$ (218.0579)
(No. 17; GUA+DMB, Table S1)</td></tr>
<tr><td colspan="4">$C_7H_8O_4$ (156.0423)
(No. 28; GUA+VL, Table S2)</td><td colspan="4">$C_{14}H_{14}O_4$ (246.0892)
(No. 1; GUA+DMB, Table S1)</td></tr>
<tr><td>60</td><td>$C_6H_4N_4$
(132.0436)</td><td>7</td><td>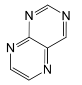</td><td colspan="4">$C_{20}H_{18}O_6$ (354.1103)
(No. 21; GUA+DMB, Table S1)</td></tr>
<tr><td>61</td><td>$C_{12}H_{14}O_5$
(238.0841)</td><td>6</td><td>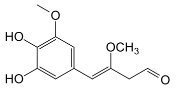</td><td colspan="4">$C_7H_{10}O_5$ (174.0528
(No. 18; GUA+DMB, Table S1)</td></tr>
<tr><td>62</td><td>$C_{13}H_{12}N_4O_5$
(304.0808)</td><td>10</td><td>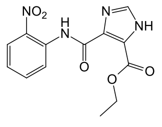</td><td>69</td><td>$C_4H_3N_3O_3$
(141.0174)</td><td>5</td><td>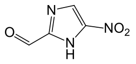</td></tr>
<tr><td colspan="4">$C_{13}H_{12}O_6$ (264.0634)
(No. 20; GUA+DMB, Table S1)</td><td colspan="4">$C_{13}H_{12}O_6$ (264.0634)
(No. 20; GUA+DMB, Table S1)</td></tr>
<tr><td colspan="4">$C_{13}H_{12}O_4$ (232.0736)
(No. 6; GUA+DMB, Table S1)</td><td>70</td><td>$C_{12}H_6N_4O_5$
(286.0338)</td><td>12</td><td>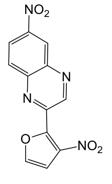</td></tr>
<tr><td>63</td><td>$C_8H_{10}N_4O$
(178.0855)</td><td>6</td><td>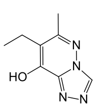</td><td>71</td><td>$C_{13}H_{12}O_5$
(248.0685)</td><td>8</td><td>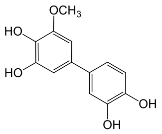</td></tr>
<tr><td>64</td><td>$C_9H_{14}N_4O$
(194.1168)</td><td>5</td><td>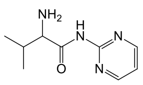</td><td>72</td><td>$C_6H_6O_4$
(142.0266)</td><td>4</td><td>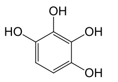</td></tr>
<tr><td>65</td><td>$C_8H_4N_4$
(156.0436)</td><td>9</td><td>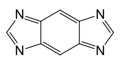</td><td colspan="4">$C_{12}H_{10}O_3$ (202.0630) (No. 33; GUA+VL, Table S2)</td></tr>
<tr><td>66</td><td>$C_{15}H_{19}N_5O_2$
(301.1539)</td><td>9</td><td>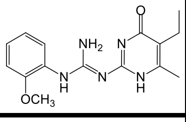</td><td>73</td><td>$C_{12}H_{12}O_4$
(220.0736)</td><td>7</td><td>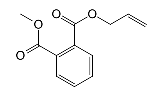</td></tr>
<tr><td>67</td><td>$C_7H_{10}N_4O_4$
(214.0702)</td><td>5</td><td>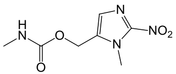</td><td colspan="4">$C_7H_6O_5$ (170.0215)
(No. 15; GUA+DMB, Table S1)</td></tr>
<tr><td colspan="4">$C_7H_8O_5$ (172.0372)
(No. 29; GUA+VL, Table S2)</td><td colspan="4">$C_7H_8O_4$ (156.0423)
(No. 28; GUA+VL, Table S2)</td></tr>
</table>

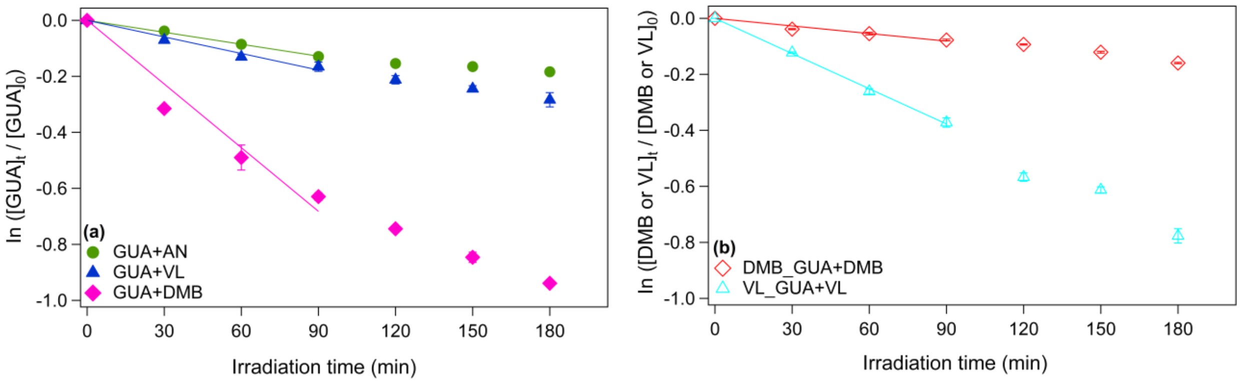

Figure S1. (a) The decay of GUA during (ammonium) nitrate-mediated photo-oxidation (GUA+AN) and photosensitized oxidation by ^{3}VL* (GUA+VL) or ^{3}DMB* (GUA+DMB). (b) The decay of DMB or VL during GUA photo-oxidation in GUA+DMB and GUA+VL, respectively. No statistically significant difference ($p > 0.05$) was noted between GUA+DMB and GUA+DMB+AN and between GUA+VL and GUA+VL+AN. Error bars represent 1 standard deviation; most error bars are smaller than the markers.

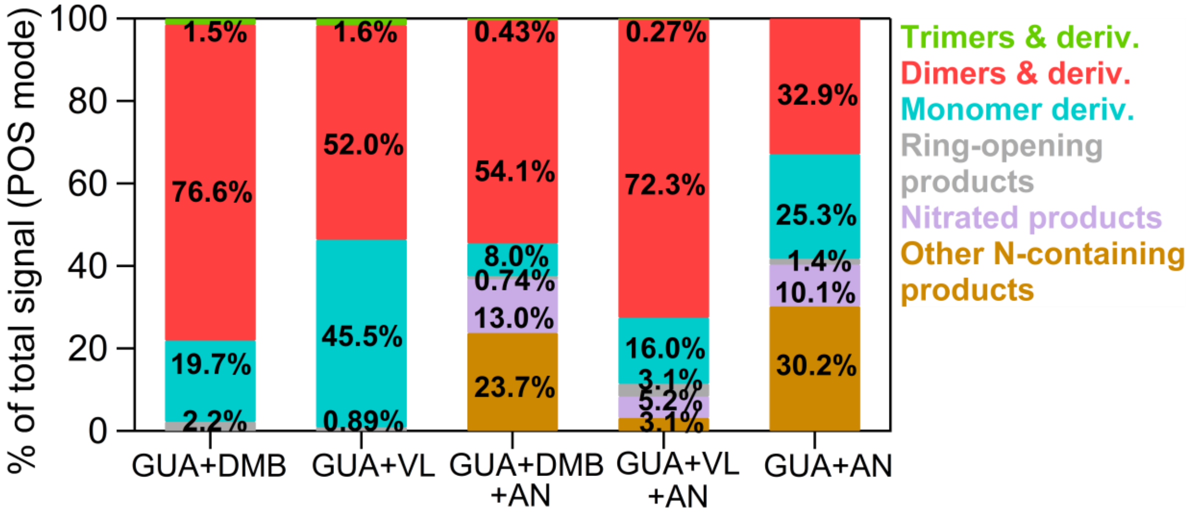

Figure S2. Signal-weighted distributions of aqSOA from GUA+DMB, GUA+VL, GUA+DMB+AN, GUA+VL+AN, and GUA+AN. These product distributions were calculated from UHPLC-HESI-Orbitrap-MS data obtained in the positive (POS) ion mode. The values indicate the contribution of different product classifications to the total signals for each reaction condition.

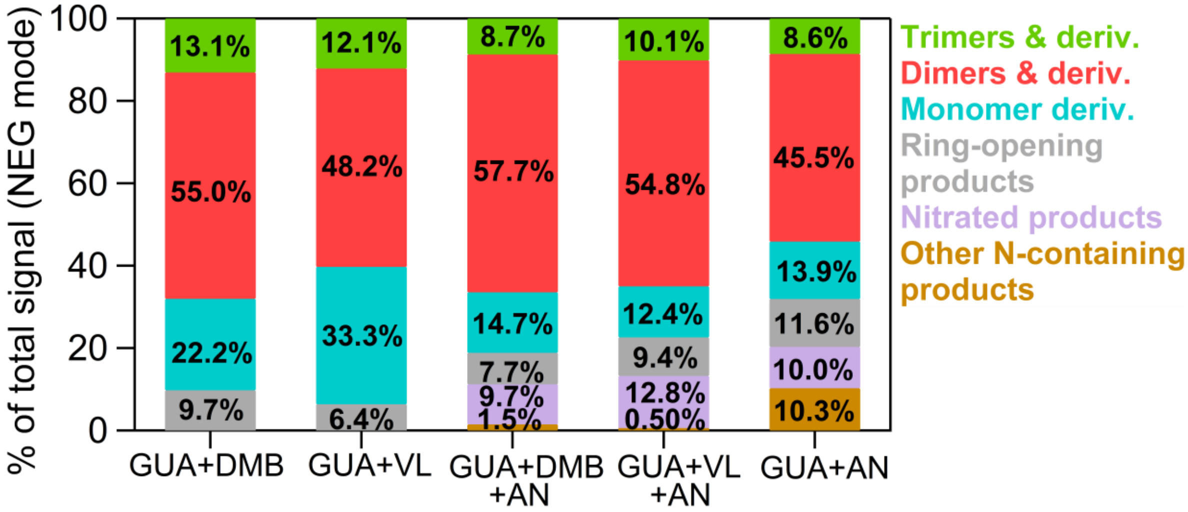

Figure S3. Signal-weighted distributions of aqSOA from GUA+DMB, GUA+VL, GUA+DMB+AN, GUA+VL+AN, and GUA+AN. These product distributions were calculated from UPLC-HESI-Orbitrap-MS data obtained in the negative (NEG) ion mode. The values indicate the contribution of different product classifications to the total signals for each reaction condition.

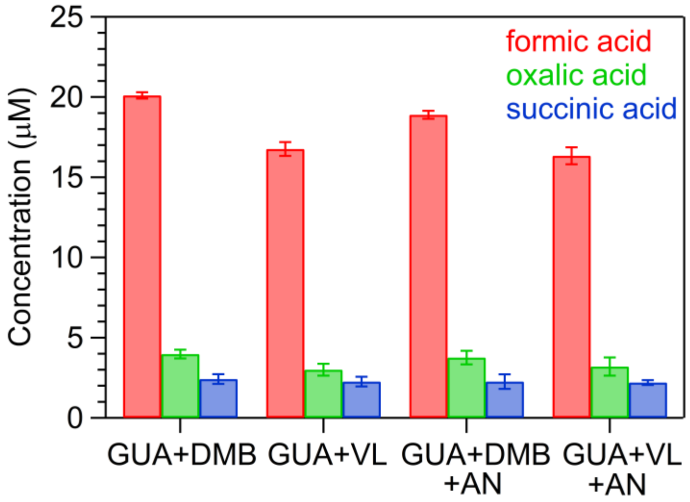

Figure S4. The concentration of formic, oxalic, and succinic acid for GUA+DMB, GUA+VL, GUA+DMB+AN, and GUA+VL+AN aqSOA. Error bars represent one standard deviation of triplicate experiments.

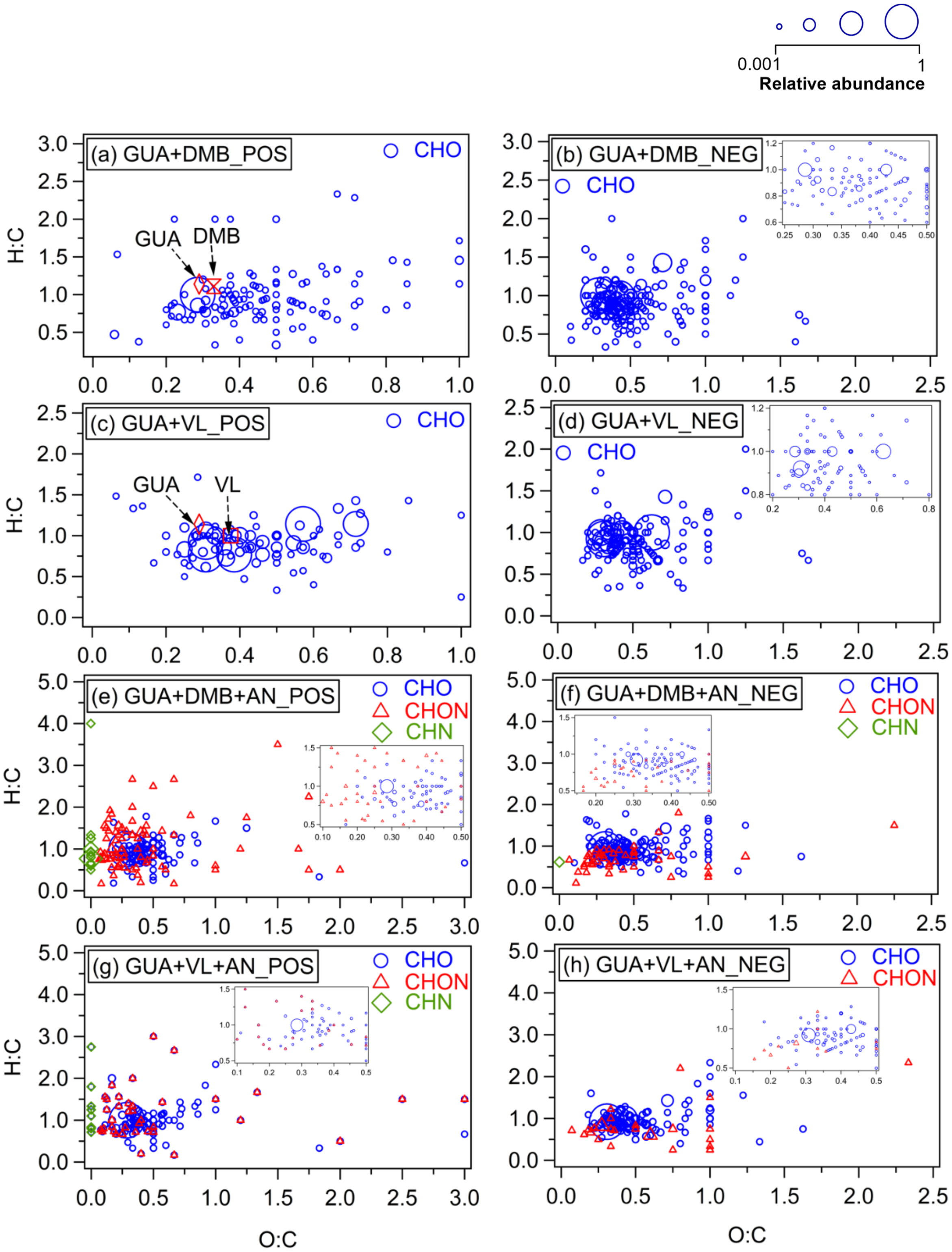

Figure S5. Van Krevelen diagrams of aqSOA from (a, b) GUA+DMB, (c, d) GUA+VL, (e, f) GUA+DMB+AN, and (g, h) GUA+VL+AN for positive (POS) and negative (NEG) ion modes. The blue circle markers indicate CHO classes, red triangle indicate CHON classes, and green diamond indicate CHN classes. The marker size reflects the relative abundance in the sample. The location of GUA, DMB, and VL in the plots are indicated only in panels a and c (red markers). The insets are expanded views of the crowded sections of the van Krevelen diagrams. Note the different scales on the axes.

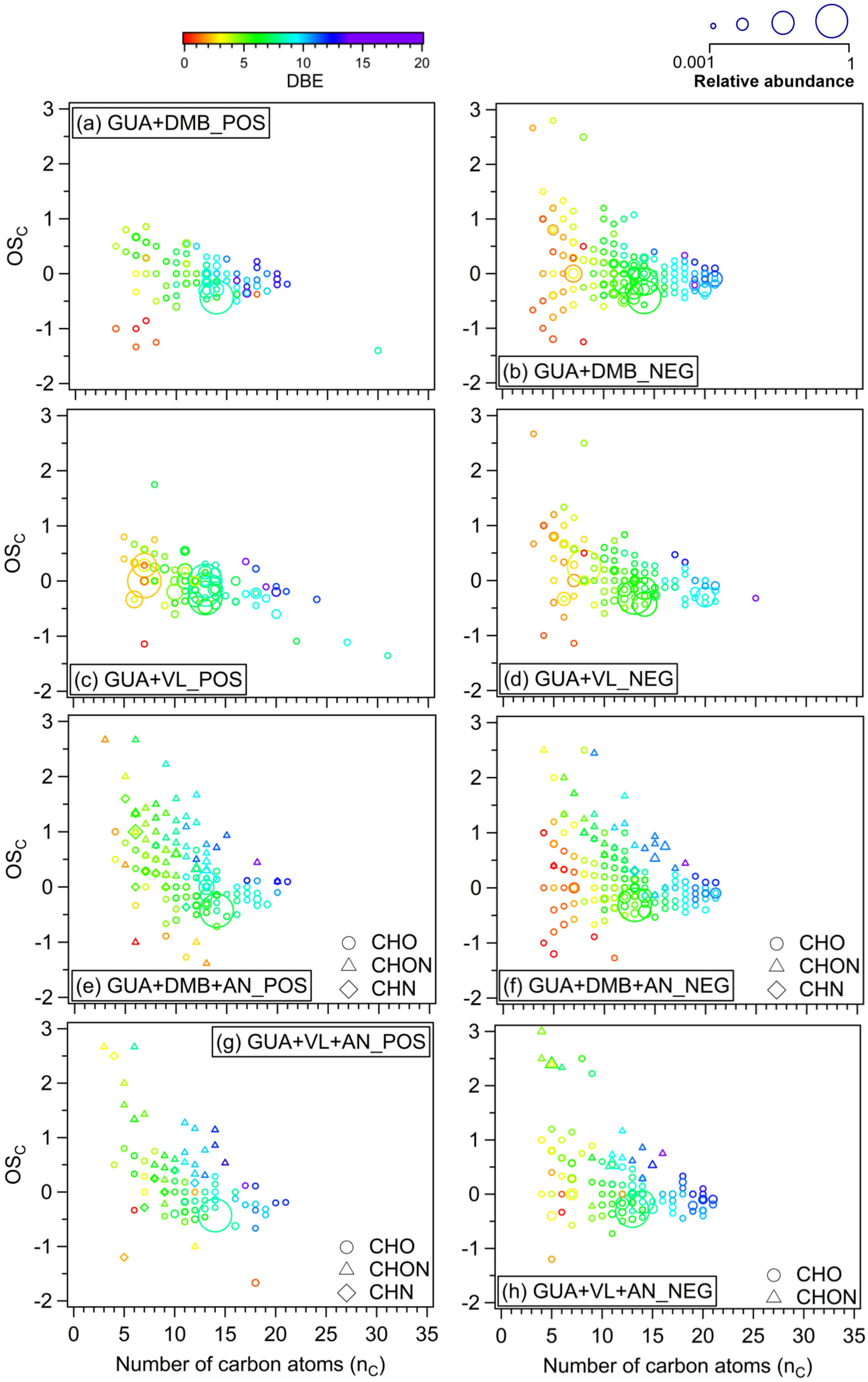

Figure S6. Plots of the carbon oxidation state (OS_C) vs. the number of carbon atoms (n_C) of aqSOA from (a, b) GUA+DMB, (c, d) GUA+VL, (e, f) GUA+DMB+AN, and (g, h) GUA+VL+AN for positive (POS) and negative (NEG) ion modes, colored by the double bond equivalent (DBE) values. The circle, triangle, and diamond markers indicate CHO, CHON and CHN classes, respectively. The marker size reflects the relative abundance in the sample.

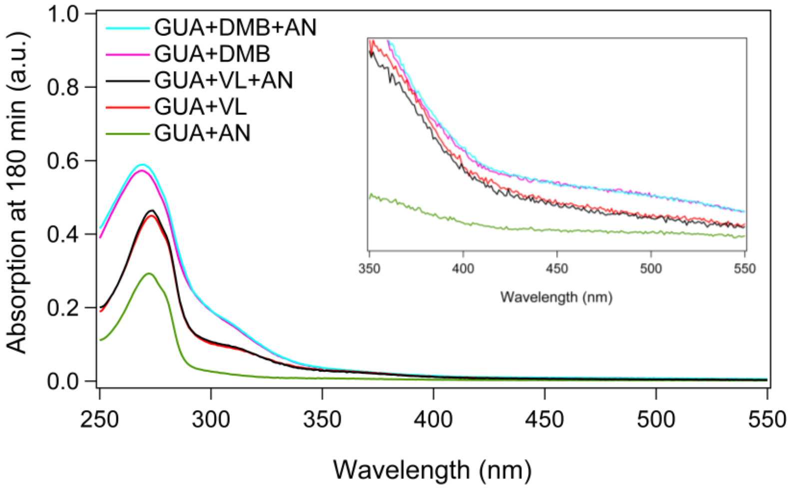

Figure S7. UV-Vis absorption spectra of GUA+DMB+AN, GUA+DMB, GUA+VL+AN, GUA+VL, and GUA+AN after 180 min of irradiation. The inset is the expanded view from 350 to 550 nm.

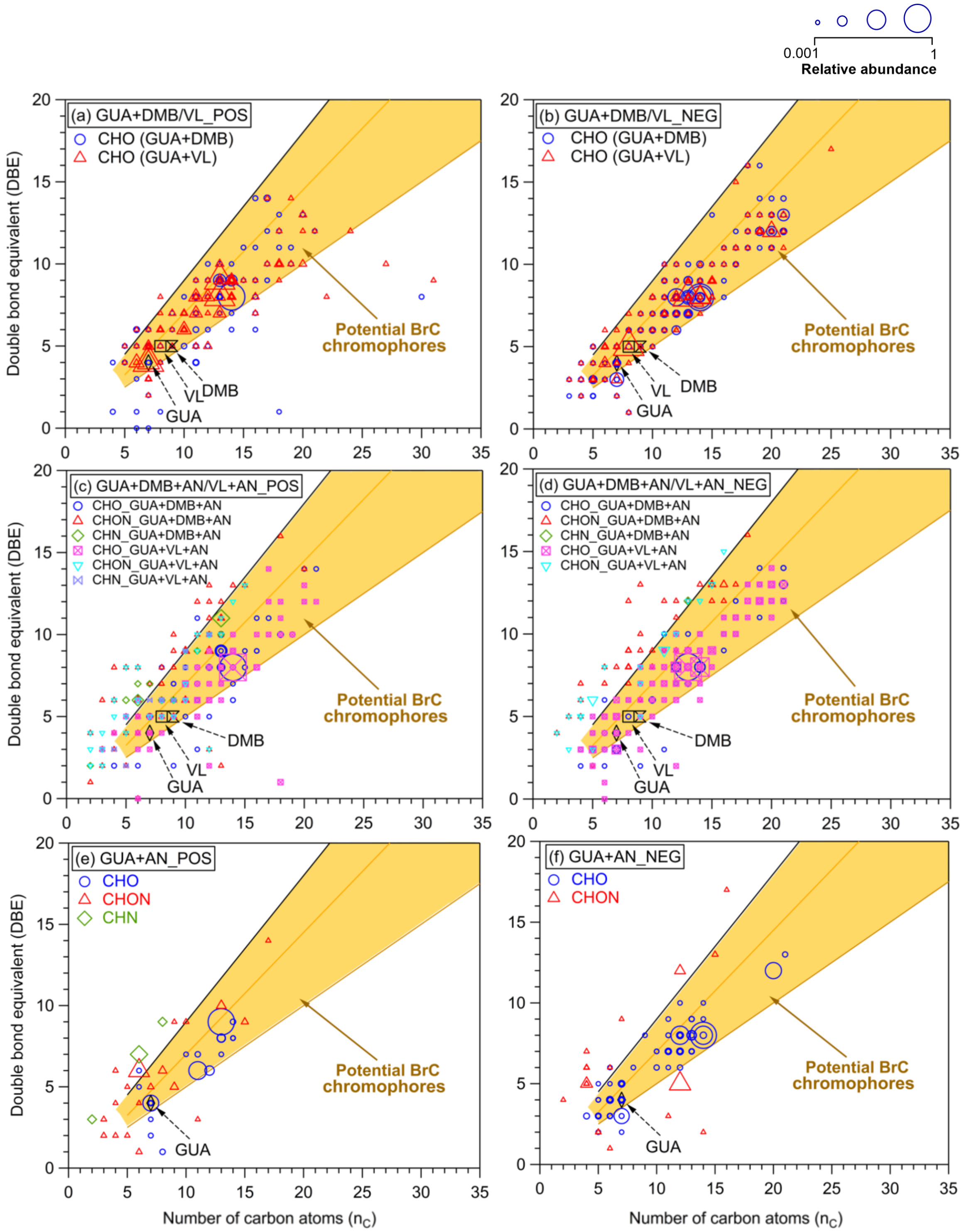

Figure S8. Plots of the double bond equivalent (DBE) values vs. the number of carbon atoms (n_C) (Lin et al., 2018) of aqSOA from (a, b) GUA+DMB and GUA+VL, (c, d) GUA+DMB+AN and GUA+VL+AN, and (e, f) GUA+AN for positive (POS) and negative (NEG) ion modes. For a and b, the blue markers indicate CHO classes for GUA+DMB and red indicate CHO classes for GUA+VL. For c and d, the blue markers indicate CHO classes, red indicate CHON classes, and green indicate CHN classes for GUA+DMB+AN; the pink markers indicate CHO classes, cyan indicate CHON classes, and purple indicate CHN classes for GUA+VL+AN. For e and f, the blue markers indicate CHO classes, red indicate CHON classes, and green indicate

CHN classes for GUA+AN. The marker size reflects the relative abundance in the sample. The three lines indicate DBE reference values of fullerene-like hydrocarbons (top, black solid line; Lobodin et al, 2012), cata-condensed polycyclic aromatic hydrocarbons (PAHs; Siegmann and Sattler, 2000) (middle, orange solid line), and linear conjugated polyenes (general formula C_xH_{x+2}) (bottom, brown solid line). Species within the shaded area are potential BrC chromophores.

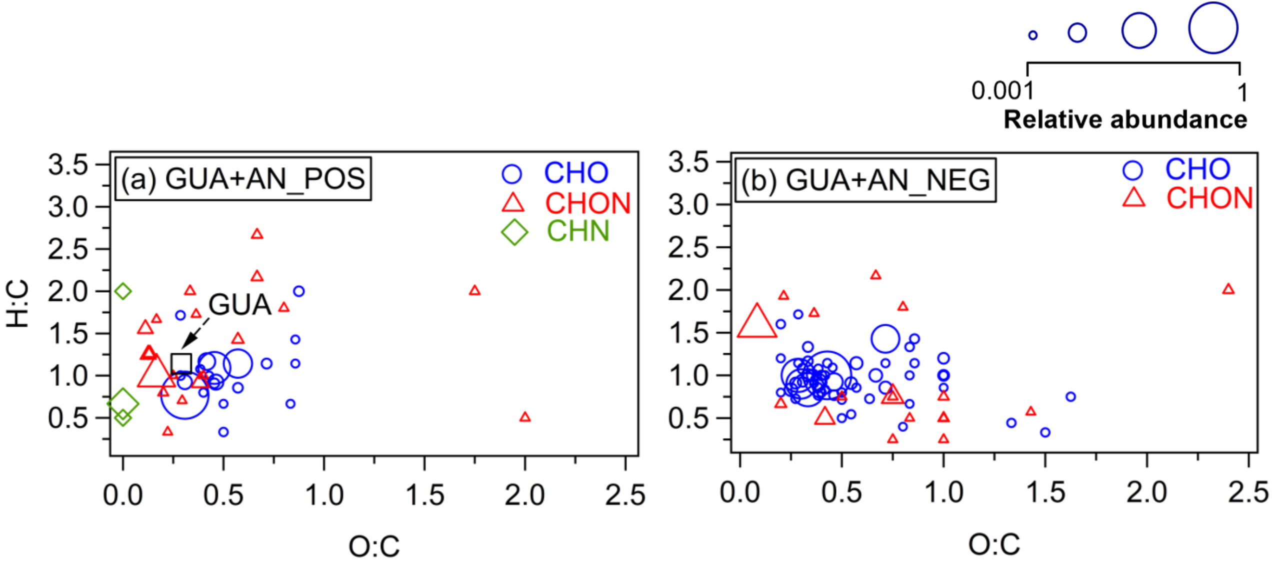

Figure S9. Van Krevelen diagrams of aqSOA from GUA+AN for (a) positive (POS) and (b) negative (NEG) ion modes. The blue markers indicate CHO classes, red indicate CHON classes, and green indicate CHN classes. The marker size reflects the relative abundance in the sample. The location of GUA is indicated only in panel a (black marker).

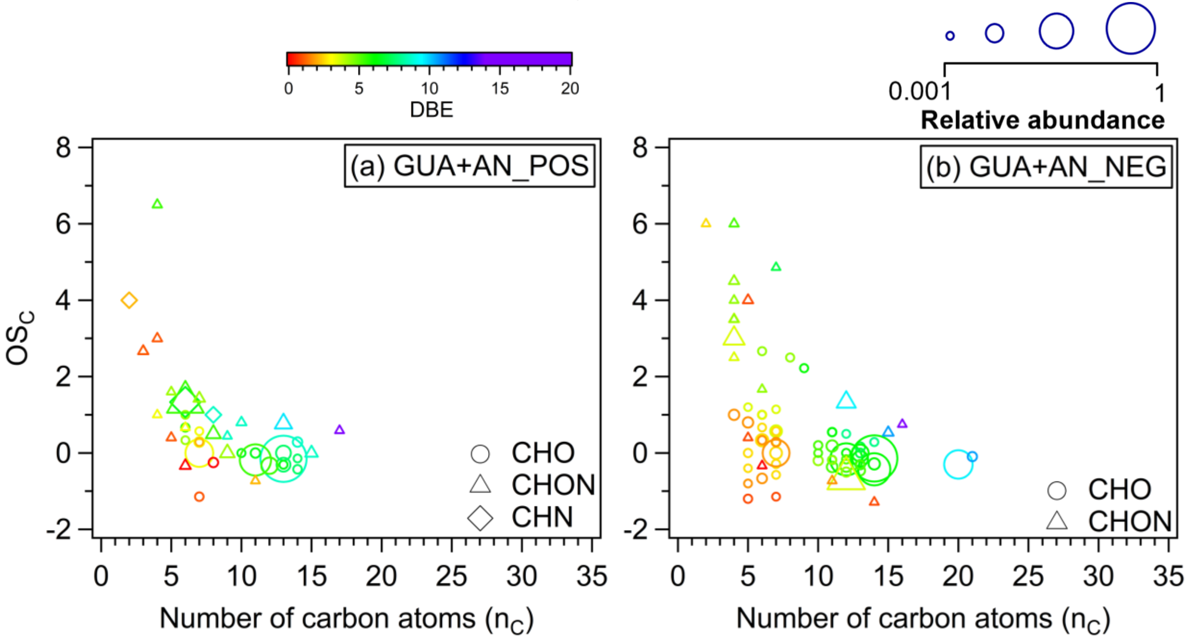

Figure S10. Plots of the carbon oxidation state (OS_C) vs. the number of carbon atoms (n_C) of aqSOA from GUA+AN for (a) positive (POS) and (b) negative (NEG) ion modes, colored by the double bond equivalent (DBE) values. The circle, triangle, and diamond markers indicate CHO, CHON and CHN classes, respectively. The marker size reflects the relative abundance in the sample.

References

Anastasio, C., Faust, B. C., and Rao, C. J.: Aromatic carbonyl compounds as aqueous-phase photochemical sources of hydrogen peroxide in acidic sulfate aerosols, fogs, and clouds. 1. Non-phenolic methoxybenzaldehydes and methoxyacetophenones with reductants (phenols), Environ. Sci. Technol., 31, 218−232, https://doi.org/10.1021/es960359g, 1997.

Bateman, A. P., Laskin, J., Laskin, A., and Nizkorodov, S. A.: Applications of high-resolution electrospray ionization mass spectrometry to measurements of average oxygen to carbon ratios in secondary organic aerosols, Environ. Sci. Technol., 46, 8315–832, https://doi.org/10.1021/es3017254, 2012.

Chen, Y., Li, N., Li, X., Tao, Y., Luo, S., Zhao, Z., Ma, S., Huang, H., Chen, Y., Ye, Z., and Ge, X.: Secondary organic aerosol formation from $^3C^*$-initiated oxidation of 4-ethylguaiacol in atmospheric aqueous-phase, Sci. Total Environ., 723, 137953, https://doi.org/10.1016/j.scitotenv.2020.137953, 2020.

Claeys, M., Vermeylen, R., Yasmeen, F., Gómez-González, Y., Chi, X., Maenhaut, W., Mészáros, T., and Salma, I.: Chemical characterization of humic-like substances from urban, rural and tropical biomass burning environments using liquid chromatography with UV/vis photodiode array detection and electrospray ionization mass spectrometry, Environ. Chem., 9, 273–284, https://doi.org/10.1071/EN11163, 2012.

He, L., Schaefer, T., Otto, T., Kroflič, A., and Herrmann, H.: Kinetic and theoretical study of the atmospheric aqueous-phase reactions of OH radicals with methoxyphenolic compounds, J. Phys. Chem. A, 123, 7828−7838, https://doi.org/10.1021/acs.jpca.9b05696, 2019.

Jiang, W., Misovich, M. V., Hettiyadura, A. P. S., Laskin, A., McFall, A. S., Anastasio, C., and Zhang, Q.: Photosensitized reactions of a phenolic carbonyl from wood combustion in the aqueous phase—chemical evolution and light absorption properties of aqSOA, Environ. Sci. Technol., 55, 5199−5211, https://doi.org/10.1021/acs.est.0c07581, 2021.

Koch, B. P. and Dittmar, T.: From mass to structure: an aromaticity index for high-resolution mass data of natural organic matter, Rapid Commun. Mass Spectrom., 20, 926–932, https://doi.org/10.1002/rcm.2386, 2006.

Kourtchev, I., Godoi, R. H. M., Connors, S., Levine, J. G., Archibald, A. T., Godoi, A. F. L., Paralovo, S. L., Barbosa, C. G. G., Souza, R. A. F., Manzi, A. O., Seco, R., Sjostedt, S., Park, J., Guenther, A., Kim, S., Smith, J., Martin, S. T., and Kalberer, M.: Molecular composition of organic aerosols in central Amazonia: an ultra-high-resolution mass spectrometry study, Atmos. Chem. Phys., 16, 11899–11913, https://doi.org/10.5194/acp-16-11899-2016, 2016.

Kroll, J. H., Donahue, N. M., Jimenez, J. L., Kessler, S. H., Canagaratna, M. R., Wilson, K. R., Altieri, K. E., Mazzoleni, L. R., Wozniak, A. S., Bluhm, H., Mysak, E. R., Smith, J. D., Kolb, C. E., and Worsnop, D. R.: Carbon oxidation state as a metric for describing the chemistry of atmospheric organic aerosol, Nat. Chem., 3, 133–139, https://doi.org/10.1038/nchem.948, 2011.

Kroll, J. H., Lim, C. Y., Kessler, S. H., and Wilson, K. R.: Heterogeneous oxidation of atmospheric organic aerosol: kinetics of changes to the amount and oxidation state of particlephase organic carbon, J. Phys. Chem. A, 119, 10767−10783, https://doi.org/10.1021/acs.jpca.5b06946, 2015.

Laskin, J., Laskin, A., Nizkorodov, S. A., Roach, P., Eckert, P., Gilles, M. K., Wang, B., Lee, H. J., and Hu, Q.: Molecular selectivity of brown carbon chromophores, Environ. Sci. Technol., 48, 12047–12055, https://doi.org/10.1021/es503432r, 2014.

Li, Y. J., Huang, D. D., Cheung, H. Y., Lee, A. K. Y., and Chan, C. K.: Aqueous-phase photochemical oxidation and direct photolysis of vanillin - a model compound of methoxy phenols from biomass burning, Atmos. Chem. Phys., 14, 2871−2885, https://doi.org/10.5194/acp-14-2871-2014, 2014.

Lin, P., Fleming, L. T., Nizkorodov, S. A., Laskin, J., and Laskin, A.: Comprehensive molecular characterization of atmospheric brown carbon by high resolution mass spectrometry with electrospray and atmospheric pressure photoionization, Anal. Chem., 90, 12493–12502, https://doi.org/10.1021/acs.analchem.8b02177, 2018.

Lobodin, V. V., Marshall, A. G., and Hsu, C. S.: Compositional space boundaries for organic compounds, Anal. Chem., 84, 3410–3416, https://doi.org/10.1021/ac300244f, 2012.

Lv, J., Zhang, S., Luo, L., and Cao, D.: Solid-phase extraction-stepwise elution (SPE-SE) procedure for isolation of dissolved organic matter prior to ESI-FT-ICR-MS analysis, Anal. Chim. Acta, 948, 55−61, https://doi.org/10.1016/j.aca.2016.10.038, 2016.

Mabato, B. R. G., Lyu, Y., Ji, Y., Li, Y. J., Huang, D. D., Li, X., Nah, T., Lam, C. H., and Chan, C. K.: Aqueous secondary organic aerosol formation from the direct photosensitized oxidation of vanillin in the absence and presence of ammonium nitrate, Atmos. Chem. Phys., 22, 273−293, https://doi.org/10.5194/acp-22-273-2022, 2022.

Misovich, M. V., Hettiyadura, A. P. S., Jiang, W., Zhang, Q., and Laskin, A.: Molecular-level study of the photo-oxidation of aqueous-phase guaiacyl acetone in the presence of $^3C^*$: formation of brown carbon products, ACS Earth Space Chem., 5, 1983−1996, https://doi.org/10.1021/acsearthspacechem.1c00103, 2021.

Schmitt-Kopplin, P., Gelencsér, A., Dabek-Zlotorzynska, E., Kiss, G., Hertkorn, N., Harir, M., Hong, Y., and Gebefügi, I.: Analysis of the unresolved organic fraction in atmospheric aerosols with ultrahigh–resolution mass spectrometry and nuclear magnetic resonance spectroscopy: organosulfates as photochemical smog constituents, Anal. Chem., 82, 8017–8026, https://doi.org/10.1021/ac101444r, 2010.

Siegmann, K. and Sattler, K.: Formation mechanism for polycyclic aromatic hydrocarbons in methane flames, J. Chem. Phys., 112, 698–709, https://doi.org/10.1063/1.480648, 2000.

Smith, J. D., Sio, V., Yu, L., Zhang, Q., and Anastasio, C.: Secondary organic aerosol production from aqueous reactions of atmospheric phenols with an organic triplet excited state, Environ. Sci. Technol., 48, 1049–1057, https://doi.org/10.1021/es4045715, 2014.

Smith, J. D., Kinney, H., and Anastasio, C.: Phenolic carbonyls undergo rapid aqueous photodegradation to form low-volatility, light-absorbing products, Atmos. Environ., 126, 36−44, https://doi.org/10.1016/j.atmosenv.2015.11.035, 2016.

Yee, L. D., Kautzman, K. E., Loza, C. L., Schilling, K. A., Coggon, M. M., Chhabra, P. S., Chan, M. N., Chan, A. W. H., Hersey, S. P., Crounse, J. D., Wennberg, P. O., Flagan, R. C., and Seinfeld, J. H.: Secondary organic aerosol formation from biomass burning intermediates: phenol and methoxyphenols, Atmos. Chem. Phys., 13, 8019–8043, https://doi.org/10.5194/acp- 13-8019-2013, 2013.

Yu, L., Smith, J., Laskin, A., Anastasio, C., Laskin, J., and Zhang, Q.: Chemical characterization of SOA formed from aqueous-phase reactions of phenols with the triplet excited state of carbonyl and hydroxyl radical, Atmos. Chem. Phys., 14, 13801−13816, https://doi.org/10.5194/acp-14-13801-2014, 2014.

Yu, L., Smith, J., Laskin, A., George, K. M., Anastasio, C., Laskin, J., Dillner, A. M., and Zhang, Q.: Molecular transformations of phenolic SOA during photochemical aging in the aqueous phase: competition among oligomerization, functionalization, and fragmentation, Atmos. Chem. Phys., 16, 4511−4527, https://doi.org/10.5194/acp-16-4511-2016.